

# Mass and charge distributions for the reaction $^{40}\text{Ca} + ^{209}\text{Bi}$ at 600 MeV

E. J. Garcia-Solis, A. C. Mignerey, H. Madani, A. A. Marchetti,\* and D. E. Russ  
*Chemistry Department, University of Maryland, College Park, Maryland 20742*

Dan Shapira

*Oak Ridge National Laboratory, Oak Ridge, Tennessee 37831*

(Received 28 February 1995)

The charge and mass of the projectile-like fragments produced in the 15-MeV per nucleon  $^{40}\text{Ca} + ^{209}\text{Bi}$  reaction were determined for products detected near the grazing angle. Neutron number-charge ( $N-Z$ ) distributions were generated as a function of the total kinetic energy loss and parametrized by their centroids, variances, and correlation coefficients. Although the initial system is very asymmetric, after the interaction, a drift of the charge and mass centroids toward further asymmetry is observed. The production of projectile-like fragments is consistent with a tendency of the projectile-like fragments to retain the projectile neutron-to-proton ratio  $\langle N \rangle / \langle Z \rangle \approx 1$ . The correlation coefficient remains well below 1.0 for the entire range of total kinetic energy lost. Predictions of two nucleon exchange models, Randrup's and Tassan-Got's, are compared to the experimental results. The models are not able to reproduce the evolution of the experimental distributions, especially the fact that the variances reach a maximum and then decrease as function of the energy loss. This behavior supports the hypothesis that some form of projectile-like fragmentation or cluster emission is perturbing the product distribution from that expected from a damped mechanism.

PACS number(s): 25.70.Lm, 25.70.Mn

## I. INTRODUCTION

A significant boundary in the description of heavy-ion collisions is the Coulomb and centrifugal barriers. When two nuclei approach each other, they must overcome these barriers to make contact. At convergent energies slightly higher than the Coulomb and centrifugal barriers, the product nuclei, in spite of the large energy conversion from relative kinetic to excitation energy, will preserve the binary character of the initial system. These kinds of reactions are termed damped or deep inelastic. Even though there have been extensive studies of these reactions, several aspects are still not completely understood. Among the open questions are two that are crucial for the understanding of the reaction mechanisms: how the excitation energy is divided between projectilelike and targetlike fragments and the direction of the drifts of the product distribution in the mass-charge plane.

It is commonly accepted that the transformation of kinetic energy and angular momentum into excitation energy and intrinsic spin of the products is caused by nucleon exchange between the two reaction partners [1,2]; however, recent experimental evidence suggests that nucleon transfer alone may not account for all of the excitation energy produced in these types of reactions [3–5]. Energy dissipation may be due to the excitation of collective surface and giant resonance modes [6]. For the case of the drifts of proton and neutron number, it has been suggested that they are driven by the static potential created by the binuclear potential [7], which would result in transfer of nucleons to produce more symmetric systems. Nevertheless, ambiguous tendencies have been observed. The study of the reaction  $^{58}\text{Ni}$  on  $^{197}\text{Au}$  at

887 MeV [8] resulted in agreement between the evolution of the drift and the predictions of the potential energy surface (PES) gradient only when equal excitation energy division between the reaction components was assumed. On the other hand, in the experiments  $^{64}\text{Ni}$  on  $^{238}\text{U}$  at 532 MeV [5],  $^{56}\text{Fe}$  on  $^{165}\text{Ho}$  at 672 MeV [9], and  $^{35}\text{Cl}$  on  $^{209}\text{Bi}$  at 528 MeV [10], the drift of the average proton and neutron numbers ( $\langle N \rangle$  and  $\langle Z \rangle$ ) does not follow the direction that minimizes the potential of the composite system.

In order to study this behavior, a quantitative analysis of the  $N-Z$  plane must be made, and characteristic parameters have to be deduced. The resemblance of the spectra to two-dimensional binomial distributions permits a description in terms of the centroids (approximated by the averages  $\langle N \rangle$  and  $\langle Z \rangle$ ), the variances  $\sigma_N^2$  and  $\sigma_Z^2$ , and the correlation coefficients  $\rho_{NZ}$  of the distributions [3]. The drifts in  $\langle N \rangle$  and  $\langle Z \rangle$  are expected to be dominated by the gradient of the binuclear potential created during the interaction time, whereas the values of the distribution variances are influenced by the multiplicity of the stochastic interchange of nucleons. On the other hand, the correlation coefficient indicates the degree of correlation in proton and neutron number for the nucleons exchanged to produce the detected projectilelike fragments. Generally,  $\rho_{NZ}$  tends to exhibit a smooth transition from uncorrelated neutron-proton exchange at values of energy loss close to zero, to correlated exchange for larger values of energy loss [5]. Finally, the  $N/Z$  equilibration is another feature of damped reactions that is usually studied. Conflicting results of the  $N/Z$  evolution as function of the energy loss have been found. For systems like  $^{64}\text{Ni} + ^{40}\text{Ca}$  at 4.5 MeV [11],  $^{37}\text{Cl} + ^{40}\text{Ca}$  at  $E/A = 12$  MeV [10], and  $^{56}\text{Fe}$  on  $^{165}\text{Ho}$  at  $E/A = 12$  MeV [9], the  $\langle N \rangle / \langle Z \rangle$  of the secondary projectilelike fragment tends to the  $N/Z$  ratio of the composite system as a function of the energy loss. On the other hand, for systems like  $^{56}\text{Fe}$  on  $^{238}\text{U}$  at  $E/A = 8.3$  MeV

\*Present address: Lawrence Livermore National Laboratory, Livermore, California 94550.

[5] and  $^{35}\text{Cl}$  on  $^{209}\text{Bi}$  at  $E/A = 15$  MeV/A [10] the  $\langle N \rangle / \langle Z \rangle$  tends to the  $N/Z$  ratio of the projectile.

To test the validity of the physical ideas used to describe the reaction mechanisms of the deep-inelastic collisions, several models have been developed. Some of these models are based on the concept of energy dissipation by collective nuclear modes [12–15], and others are supported by the hypothesis of stochastic exchange of nucleons between the colliding ions [16–20]. Given that the distributions predicted by the models often describe the emitted fragments in their excited state after the interaction, and that the experimental data are from secondary fragments, evaporation corrections usually have to be taken into account to make comparisons between experimental data and model predictions.

Generally, the collective models lack consistency and completeness. Because of their restriction to particular aspects of the reaction mechanisms and their dependence on relevant features by auxiliary theories, it is difficult to judge the precision of the basic concepts that these models propose [21]. Over all, the nucleon-exchange models are better able to reproduce the characteristics of the damped reactions. Based on stochastic transport theories, most of these models predict the evolution of the  $N$ - $Z$  centroid distributions, as well as their variances, in a mode suitable for comparison with experiments.

In this work, the secondary mass and charge distributions of the projectilelike fragments of the system  $^{40}\text{Ca}$  on  $^{209}\text{Bi}$  at  $E/A = 15$  MeV were measured. The study is focused on the limits and characteristics of the damped reactions at this energies. Special emphasis is given in this work to the effects of the dynamic and static driving forces on the product distribution in the mass-charge plane. It is also discussed in this paper how the excitation energy is divided between projectilelike and targetlike fragments. The wide range of energy loss produced in this reaction can provide additional information of the evolution of the energy division process as compared to measurements of similar systems reported so far [10,16]. On the other hand, given the closed-shell nature of the projectile, the system studied is ideal to explore the influence of the nuclear structure on the nucleon drifts [18]. Finally, the asymmetric character of the system under study, together with the aspects mentioned above, allow for detailed tests of nucleon exchange models.

The experimental setup and the details of the data acquisition and reduction are given in Sec. II, which is followed by a presentation of the experimental results and the evaporation corrections in Sec. III. The comparison to model predictions and other systems is made in Sec. IV. Finally, a summary and the final conclusions are given in Sec. V.

## II. EXPERIMENT AND DATA REDUCTION

The experiment was performed at the Holifield Heavy-Ion Research Facility (HHIRF) of Oak Ridge National Laboratory. A 598-MeV  $^{40}\text{Ca}$  beam was used to produce the reaction on a self-supporting  $^{209}\text{Bi}$  (1 mg/cm<sup>2</sup>) target. The beam charge current was kept between 10 and 15 nA during the experiment. The projectilelike fragments were detected at a laboratory angle of 9.35° using time of flight (TOF) to identify their mass number and a  $\Delta E$ - $E$  system to deduce their atomic number and kinetic energy.

The experiment was performed in a 30.5-cm-diameter scattering chamber connected to a TOF arm. The start and stop detectors were transmission-type parallel plate avalanche counters (PPAC's). In addition to timing information, the stop PPAC was used to provide position in the detection plane. The  $\Delta E$ - $E$  energies of the projectilelike fragments were measured using a gas ionization chamber, which was segmented into four anodes. The data were collected using the CAMAC data acquisition system [22], and the off-line data analysis was performed using the program LISA [23]. This study was part of a series of similar experiments; a detailed description of the setup may be found in Refs. [9,10].

The kinetic energy calibration of the projectilelike fragments was performed using elastic events. The gains of the first, second, and fourth elements of the ionization chamber  $\Delta E_i$ ,  $i=1,2,4$ , were normalized to that of the third element  $\Delta E_3$ . The absolute calibration was fixed by equating the sum of the relative energies from the four  $\Delta E$  elements to the energy computed with STOPX [23], a stopping power program. It was found that the measured  $\Delta E$  energies had a dependence on the position where the projectilelike fragments (PLF's) hit the detector surface ( $X$ - $Y$ ) perpendicular to the beam direction ( $Z$ ). Because of this dependence, corrections to the  $\Delta E$  signals, and thus to the total energy ( $E_{\text{tot}}$ ), were made.

The dependence on the  $X$  and  $Y$  positions of the energy deposited by the elastic events in each  $\Delta E_i$  was fit to a polynomial for each direction, that is, one for the  $\Delta E_i$  vs  $X$  dependence and other for the  $\Delta E_i$  vs  $Y$  dependence. Then, using the coefficients of the polynomials, the correction for kinetic energy for the rest of the events was performed. After this correction, the total energy was calculated ( $E_{\text{tot}} = \sum_{i=1}^4 \Delta E_i$ ). Because after this first attempt the energy still had some position dependence, another correction was made to account for the two-dimensional  $X$ - $Y$  dependence.

The energy spectrum can be thought as a plane of  $X$ - $Y$  coordinates containing the Ca elastic centroid values. Based on these coordinates, one matrix with the number of elastic counts and another with the energy values can be computed. Then the first moment of the centroid matrix  $E_{\text{elastic}}(X, Y)$  may be found by the relation

$$E_{\text{elastic}}(X, Y) = \frac{\sum_i E_i(X, Y)}{\sum_i N_i(X, Y)}, \quad (1)$$

where  $N_i$  is the number of events in any  $X$ - $Y$  bin and  $E_i$  is the elastic value for the same bin. Using this energy-position matrix, the projectilelike fragment energy was adjusted by normalizing to a single channel value using

$$E_{\text{PLF}}(X, Y) = \frac{E'_{\text{PLF}}(X, Y)}{E_{\text{elastic}}(X, Y)} E_{\text{tot}}, \quad (2)$$

where  $E_{\text{PLF}}$  and  $E'_{\text{PLF}}$  are the corrected and noncorrected energy of the PLF's, respectively, and  $E_{\text{tot}}$  represents the absolute energy value calculated for the elastic events.

The values of the TOF also had an  $X$ - $Y$  dependence, due in part to the disparity of the electromagnetic field within the detector, and also due to the different path lengths over the face of the stop detector. So a matrix correction was again

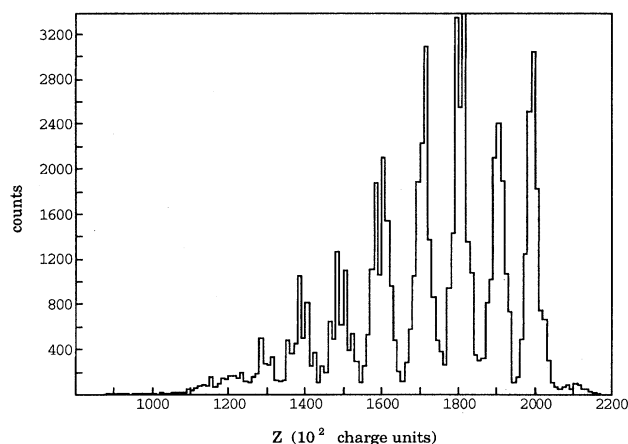


FIG. 1. The measured charge distribution for the projectilelike fragments. The elastic peak has been suppressed.

employed. The resolution for the total energy and time of flight after corrections was calculated by the full width at half maximum (FWHM) for the elastic peak, giving  $\delta E_{\text{tot}} \approx 12.6$  MeV and  $\delta \text{TOF} \approx 849$  ps.

The atomic number identification was done following the  $\Delta E$ - $E$  technique. The series of curves ( $Z$  curves) from the  $\Delta E$  vs  $E$  plane were mapped until the charge values were independent of the fragment energy. The second element of the ionization chamber was used as the  $\Delta E$ , and so events that stopped in the first or second element of the ionization chamber were not considered for the data analysis, setting a cut off in the energy of 10 MeV for Ca products. The calibration was set by a polynomial fit based on the  $Z$  of Ca. The resolution achieved for the charge using the FWHM of the elastic peak was  $\delta Z \approx 0.36$  charge units. The resulting charge distribution is shown in Fig. 1.

Since the mass of a projectilelike fragment is proportional to its kinetic energy times the square of the time of flight, the determination of the mass is, in principle, a simple task. However, because of the resolution obtained for the time of flight, the elastic mass resolution was about 1.3 mass units. In consequence, the centroid positions of the mass spectrum could not be established with certainty, as shown in Fig. 2(a), where the PLF mass distributions are plotted for  $Z=18$ .

By setting a window for each  $Z$ , projections on the mass axis were made for energy intervals of about 15 MeV. The positions of the mass peaks were then established by deconvolution of the spectra [24], and the mass number was calibrated by a quadratic function using the elastic peak as absolute reference. The distribution of the resulting mass for PLF's with  $Z=18$  is shown in Fig. 2(b). The individual mass centroids are as indicated. There is good agreement between the mass values for adjacent charges. However, it is important to note that the deconvolution procedure was used with the purpose of calibrating the mass parameter for each  $Z$ . Therefore, in principle this procedure could introduce an uncertainty in the mass of one unit when matching the mass peaks from one  $Z$  spectrum to another, especially for the fragments with charges far from the elastic.

Once the mass number, the charge, and the kinetic energy of the secondary projectilelike fragments were established,

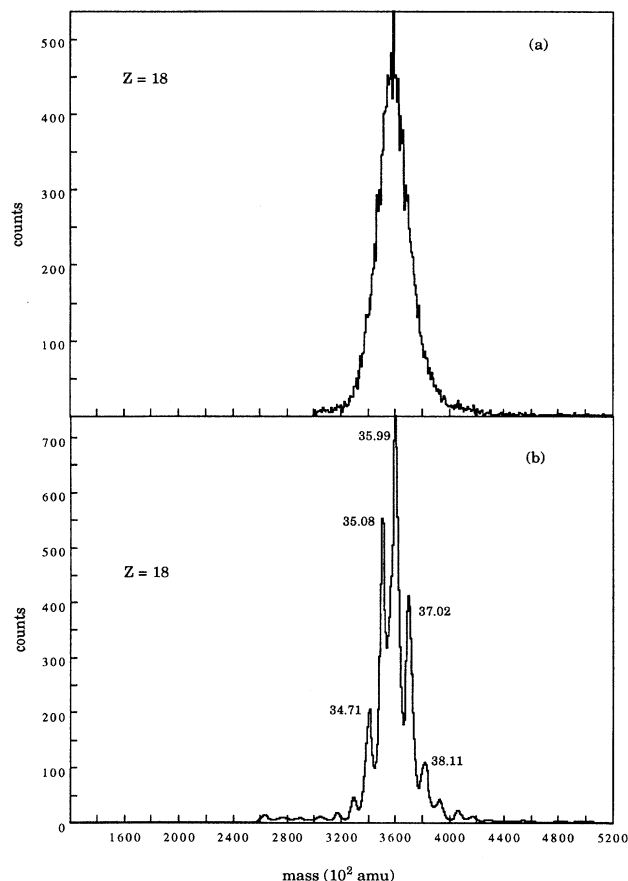


FIG. 2. Measured mass distribution for the projectilelike fragments with  $Z=18$ . (a) After the correction of the energy and TOF  $X$ - $Y$  dependence. (b) After the correction using the deconvolution technique. The centroids of the dominant mass peaks identified are as indicated.

the computation of the total kinetic energy lost (TKEL) in the reaction was performed [9,10]. Because of the particle evaporation of the excited primary products, the measured mass differed from the primary mass and it was necessary to introduce a correction to the mass of the measured PLF's. Two possibilities were considered for the excitation energy parameter when running the evaporation corrections. In the first case, it was supposed that there was an equal energy division of the total available excitation energy  $E_{\text{tot}}^*$  between the PLF and the TLF ( $E_{\text{PLF}}^* = E_{\text{TLF}}^*$ ). In the second case, the two fragments were assumed to reach statistical equilibrium; therefore,  $E_{\text{tot}}^*$  was divided between the reaction fragments in proportion to their mass ratios, as given by the equation

$$E_{\text{PLF}}^* = E_{\text{TLF}}^* \frac{M_{\text{PLF}}}{M_{\text{TLF}}}. \quad (3)$$

For each event, the procedure to correct the TKEL was done using the iteration method described extensively in other studies [9,10], with the difference that the evaporation correction was performed, not only by increasing the mass of the secondary PLF ( $\delta M$ ), but also by increasing its charge value ( $\delta Z$ ).

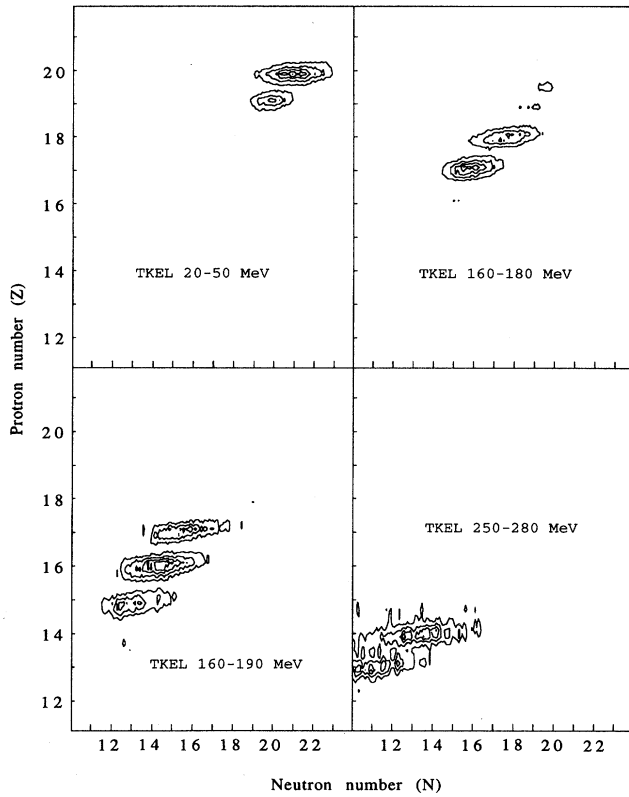


FIG. 3. Representative contour plots of the measured atomic number ( $Z$ ) versus the measured neutron number ( $N$ ) for four different bins of TKEL: 20–50 MeV, 100–130 MeV, 160–190 MeV, and 250–290 MeV.

The evaporation functions  $\delta M = \delta M(Z, M, E_{\text{PLF}}^*)$  and  $\delta Z = \delta Z(Z, M, E_{\text{PLF}}^*)$  were calculated using the projection angular-momentum coupled evaporation code PACE II [25]. Except for the spin and the angular momentum, the default values of the program were used. Calculations have shown that the amounts of charge and mass evaporated are not strongly dependent of the spin values [26]. Therefore, only an estimate of the initial spin of the primary PLF was used. On the other hand, the angular momentum of the PLF was computed assuming the classical sticking model, using a linear interpolation between its higher (grazing) and lower (fusion) limits [26,27].

After the TKEL corrections were performed, the  $N$ - $Z$  distributions were generated by plotting the relative yield of projectilelike fragments as a function of their atomic and neutron numbers. Examples of the distributions for different cuts of total kinetic energy loss are displayed in Fig. 3. The  $N$ - $Z$  plane is binned in cells of  $0.20 \times 0.18$  neutron-charge units. The contour lines in Fig. 3 represent a linear scale, and the lines indicate events with 90%, 70%, 50%, 30%, and 10% of the maximum yield of each distribution.

The resemblance of the spectra to two-dimensional binomial distributions allows the parametrization of the  $N$ - $Z$  plane in terms of centroids, variances, and correlation coefficients [5]. Employing consecutive 10- to 30-MeV bins of TKEL, moment analysis was used to calculate the parameters:

$$\langle Z \rangle = \frac{1}{n} \sum_{i=1}^n Z_i \quad (4)$$

and

$$\sigma_Z^2 = \frac{1}{n-1} \sum_{i=1}^n (Z_i - \langle Z \rangle)^2. \quad (5)$$

Analogous equations were used for the neutron number. The correlation factor is given by

$$\rho_{NZ} = \frac{\sigma_{NZ}}{\sigma_N \sigma_Z}, \quad (6)$$

with

$$\sigma_{NZ} = \frac{1}{n-1} \sum_{i=1}^n (Z_i - \langle Z \rangle)(N_i - \langle N \rangle). \quad (7)$$

The population of the distributions for the bins of TKEL used to calculate the parametrization went from 10 000 events for the bin TKEL, 0–20 MeV, to 40 events for the bin TKEL, 380–420 MeV. The resulting parameters are summarized in Tables I and II. Corrections for finite resolution derived from the experimental distributions were made. The uncertainties were calculated by the statistical error propagation method.

### III. EXPERIMENTAL RESULTS

Graphical representation of the experimental parameters given in Tables I and II are shown in Figs. 4 and 5. The squares represent the correction of the TKEL assuming thermal equilibrium of the primary fragments and the circles represent the correction assuming equal energy division. If the error bars in the figures were smaller than the plot symbols, they were not included. Also in Fig. 4, the uncertainty associated with the possible mismatch of one mass unit coming from the method used to resolve the mass for charges far from the projectile (as explained in Sec. I) is represented for  $\langle N \rangle$  and  $\langle N \rangle / \langle Z \rangle$  at 360 MeV. Finally, it should be noted that the arrows displayed in Figs. 4, 5 (and Fig. 7, below) indicate the TKEL corresponding to the entrance channel Coulomb barrier, which is 324 MeV for this system. This serves only as a guide since in this region of fully damped events a lowering of the Coulomb barrier is expected from the deformation of products. In addition decay via sequential breakup as opposed to particle evaporation may be possible.

As can be seen in Fig. 4, the  $\langle Z \rangle$  and  $\langle N \rangle$  decrease with increasing energy loss for both cases of TKEL correction. The  $\langle N \rangle / \langle Z \rangle$  ratio remains around 0.9 for all the TKEL values, well below the ratio of the composite system (1.4). Around 170 MeV of TKEL,  $\langle Z \rangle$  and  $\langle N \rangle$  have lost about 5  $Z$  and 7  $N$  units, respectively. At low energy loss, the differences between the  $\langle Z \rangle$  and  $\langle N \rangle$  corresponding to the two types of TKEL correction are not significant; however, around 80 MeV of TKEL these differences increase slightly. The thermal equilibrium correction yields average values of charge and neutron number that are larger than those obtained by the equal energy division correction. This result is expected since the equal division of excitation energy will

TABLE I. The secondary centroids  $\langle Z \rangle$  and  $\langle N \rangle$ , the variances  $\sigma_Z^2$  and  $\sigma_N^2$ , and correlation factor  $\rho_{NZ}$ , for the secondary distributions obtained from the reaction  $^{40}\text{Ca}+^{209}\text{Bi}$  at 600 MeV. The energy-loss scale TKEL has been corrected for evaporation assuming equal excitation energy division between the reaction fragments. The TKEL values of the center of the bin are quoted and reflect consecutive bin intervals.

TKEL	$\langle Z \rangle$	$\langle N \rangle$	$\langle N \rangle / \langle Z \rangle$	$\sigma_Z^2$	$\sigma_N^2$	$\rho_{NZ}$
15	19.88±0.04	21.18±0.01	1.066±0.002	0.152±0.023	1.505±0.260	0.259±0.035
45	19.37±0.01	20.17±0.01	1.041±0.001	0.428±0.016	3.067±0.373	0.373±0.012
65	19.91±0.01	19.26±0.01	1.019±0.002	0.632±0.027	3.522±0.424	0.423±0.017
75	18.69±0.01	19.05±0.01	1.019±0.001	0.640±0.028	3.955±0.402	0.402±0.016
85	18.17±0.02	17.93±0.01	0.987±0.001	0.536±0.028	2.919±0.429	0.428±0.018
95	18.87±0.01	17.26±0.01	0.966±0.001	0.394±0.021	2.084±0.435	0.435±0.019
105	17.56±0.01	16.87±0.01	0.960±0.001	0.737±0.028	2.494±0.543	0.543±0.018
115	17.21±0.01	16.37±0.01	0.951±0.002	0.757±0.030	2.934±0.508	0.508±0.017
135	16.38±0.01	15.26±0.01	0.931±0.001	1.135±0.025	4.118±0.525	0.525±0.013
165	15.38±0.01	14.21±0.01	0.924±0.001	1.479±0.036	4.775±0.556	0.556±0.015
200	14.36±0.01	13.08±0.01	0.911±0.002	1.260±0.043	6.109±0.454	0.454±0.017
240	13.06±0.02	12.00±0.02	0.919±0.003	0.965±0.059	6.513±0.385	0.385±0.023
280	11.69±0.04	11.49±0.05	0.983±0.008	0.585±0.091	7.077±0.288	0.288±0.037
320	10.20±0.10	9.37±0.11	0.919±0.021	0.706±0.185	4.289±0.406	0.406±0.110
360	9.55±0.38	8.40±0.56	0.879±0.094	0.259±0.471	4.184±0.249	0.249±0.372
400	8.72±0.78	7.69±1.03	0.881±0.262	0.026±0.726	0.751±0.639	0.639±0.472

deposit more excitation in the lighter PLF for the same TKEL than will the thermal division, causing the increased effect of evaporation of the primary products.

The values of  $\sigma_Z^2$ ,  $\sigma_N^2$ , and  $\rho_{NZ}$  are displayed in Fig. 5. The general development of these parameters as a function of the TKEL is similar for the equal excitation energy division and the thermal equilibrium corrections. The  $\sigma_Z^2$  increases to around 1.8 at TKEL of 200 MeV and then starts decreasing until about 320 MeV of energy loss. After this point the trend of the data is not clear, because the maximum TKEL imposed by the spherical entrance channel Coulomb

barrier is 324 MeV (indicated by the arrow). While products of different charge and deformation will have different barriers, this value serves as a guide for the expected limit for the deep-inelastic products. In general  $\sigma_N^2$  follows the same pattern as  $\sigma_Z^2$ ; however, its overall value and its rate of increase are larger. Starting at around 2 for 20 MeV of TKEL,  $\sigma_N^2$  reaches a maximum at around 300 MeV of TKEL. Some kind of discontinuity is present around 50 MeV of TKEL, especially for values of  $\sigma_N^2$ . It is interesting to note that this energy is in the same region where a change in the slope of  $\langle Z \rangle$  and  $\langle N \rangle$  is observed.

TABLE II. The secondary centroids  $\langle Z \rangle$  and  $\langle N \rangle$ , the variances  $\sigma_Z^2$  and  $\sigma_N^2$ , and correlation factor  $\rho_{NZ}$ , for the secondary distributions obtained with the reaction  $^{40}\text{Ca}+^{209}\text{Bi}$  at 600 MeV. The energy-loss scale TKEL has been corrected for evaporation assuming thermal division of excitation energy between the reaction fragments. The values of the center of the bin are quoted and reflect consecutive bin intervals.

TKEL	$\langle Z \rangle$	$\langle N \rangle$	$\langle N \rangle / \langle Z \rangle$	$\sigma_Z^2$	$\sigma_N^2$	$\rho_{NZ}$
15	19.90±0.03	21.12±0.03	1.062±0.003	0.216±0.050	1.705±0.118	0.327±0.055
45	19.45±0.01	20.19±0.01	1.038±0.001	0.377±0.022	2.073±0.053	0.426±0.018
65	19.20±0.02	19.67±0.02	1.025±0.002	0.481±0.028	2.311±0.074	0.456±0.020
75	18.74±0.01	19.05±0.01	1.015±0.002	0.590±0.029	3.019±0.091	0.442±0.017
85	18.47±0.01	18.52±0.01	1.004±0.001	0.668±0.030	3.687±0.099	0.426±0.016
95	18.17±0.01	17.81±0.01	0.980±0.002	0.664±0.033	2.996±0.082	0.471±0.017
105	17.94±0.01	17.41±0.01	0.970±0.002	0.803±0.038	2.887±0.080	0.527±0.018
115	17.74±0.01	17.12±0.01	0.965±0.002	0.985±0.024	3.082±0.086	0.565±0.019
135	17.04±0.01	16.10±0.01	0.945±0.001	1.061±0.034	3.692±0.066	0.536±0.012
165	16.38±0.01	15.10±0.01	0.922±0.001	1.396±0.040	4.692±0.093	0.545±0.015
200	15.28±0.01	14.12±0.01	0.924±0.001	1.669±0.042	5.454±0.103	0.553±0.015
240	14.18±0.01	12.61±0.01	0.889±0.002	1.115±0.046	6.316±0.163	0.420±0.017
280	13.09±0.02	12.04±0.02	0.919±0.003	0.720±0.073	7.012±0.265	0.320±0.020
320	11.97±0.04	11.78±0.04	0.984±0.007	0.533±0.288	6.998±0.403	0.276±0.032
360	10.53±0.08	9.83±0.09	0.933±0.016	0.703±0.160	5.098±0.761	0.371±0.083
400	9.52±0.20	8.38±0.25	0.881±0.045	0.388±0.288	4.798±1.455	0.285±0.177

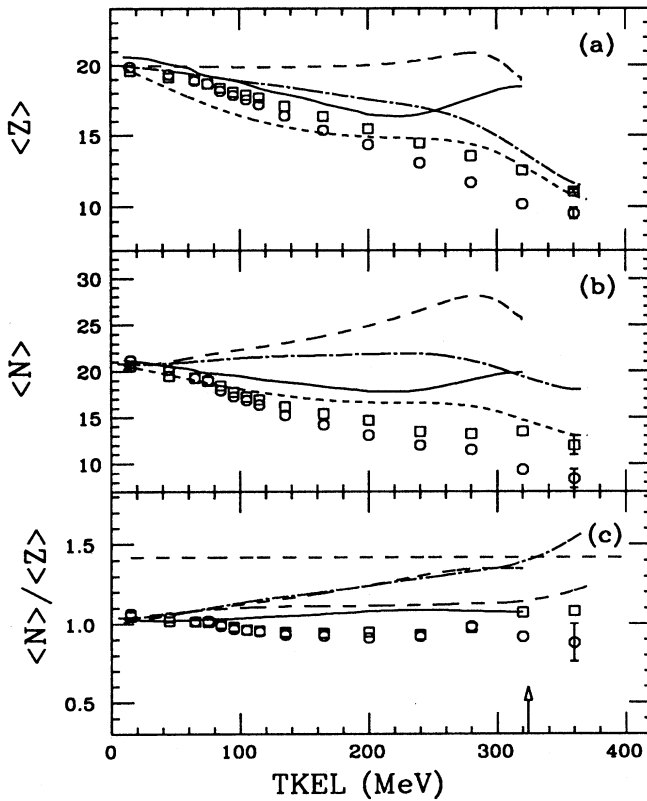


FIG. 4. Experimental and theoretical values of  $\langle Z \rangle$ ,  $\langle N \rangle$ , and  $\langle N \rangle / \langle Z \rangle$  corresponding to the secondary distributions of the projectilelike fragments. The circles and squares represent the experimental results after correcting the energy-loss scale, assuming equal and thermal division of the excitation energy, respectively. The theoretical results predicted by Randrup's and the Tassan-Got-Stéphan models are represented by lines. The dashed lines and the dash-dotted lines represent the result of the primary distributions predictions by Randrup's and the Tassan-Got-Stéphan models, respectively. The solid lines represent the results from Randrup's model, and the dotted lines represent the results from the Tassan-Got-Stéphan model after being corrected for evaporation using PACE II. The arrow indicates the limit imposed by the entrance channel spherical-Coulomb barrier.

The correlation coefficient  $\rho_{NZ}$  is about 0.3 at 20 MeV of TKEL. It then increases to its maximum of 0.6 at 180 MeV of TKEL, after which it decreases slowly. Although the evaporation process disturbs the significance of the  $\rho_{NZ}$ , a small correlation between the proton and neutron exchange may be inferred from the observed trend. As for the  $\rho_{NZ}$  decreasing, in the nucleon transfer picture this tendency does not make sense, given that it would mean that as more neutrons are transferred to the PLF less protons are transferred, or vice versa. Therefore, this trend may be interpreted as an evidence that some other reaction mechanism starts taking place at this point in the reaction.

#### IV. MODEL CALCULATIONS AND COMPARISON TO OTHER SYSTEMS

Two nucleon exchange models have been used to interpret the experimental results: Randrup's model [18] and the Tassan-Got-Stéphan model [19]. In these calculations, the physical picture of the reaction is generally the same. The projectile and target approach each other along Coulomb trajectories until they are within the interaction radius. At this point the system is represented as two Fermi-Dirac gases which exchange nucleons, energy, and angular momentum. After the interaction, the primary PLF and TLF follow separate Coulomb trajectories and decay by evaporation into secondary residues.

The models utilize different approaches to determine the nucleon transfer. For the Tassan-Got-Stéphan model, when the participant nuclei are within range of their potential, a

window opens and stochastic transfers may occur. The transfer probability is calculated via a phase-space integral, which, accounting for the Pauli blocking, incorporates the phase-space flux term, the barrier penetrability, and the occupation probabilities. This transfer produces the variation of mass, charge, excitation energy, and spin. On the other hand, in Randrup's model, the dynamical variables are determined by treating the interacting nuclei as two spheres interconnected by a small cylindrical neck. The mean trajectory of these variables is derived from the Lagrange-Rayleigh equations of motion and the fluctuations are found using a Fokker-Planck-type transport equation. Nucleon-nucleon collisions are mostly prohibited by the Pauli principle, and so the relative angular momenta are generated via the interaction of the system with the mean field.

Among the differences between Randrup's model and the Tassan-Got-Stéphan model is the way that the Fermi levels are calculated in each approach. In Randrup's model the Fermi levels are extracted from the Lagrangian of the system. On the other hand, in the Tassan-Got-Stéphan formulation the Fermi levels are determined for each nucleus independently as separation energies computed from mass tables. This may result in a faster equilibration of temperature between the participant nuclei in the predictions from the Randrup's model, as compared to the Tassan-Got-Stéphan formulation [19]. Also, a larger amount of excitation energy may be produced during the interaction according to Randrup's approach.

The presence of an interaction energy in the Lagrangian used in Randrup's model is another factor that causes a sig-

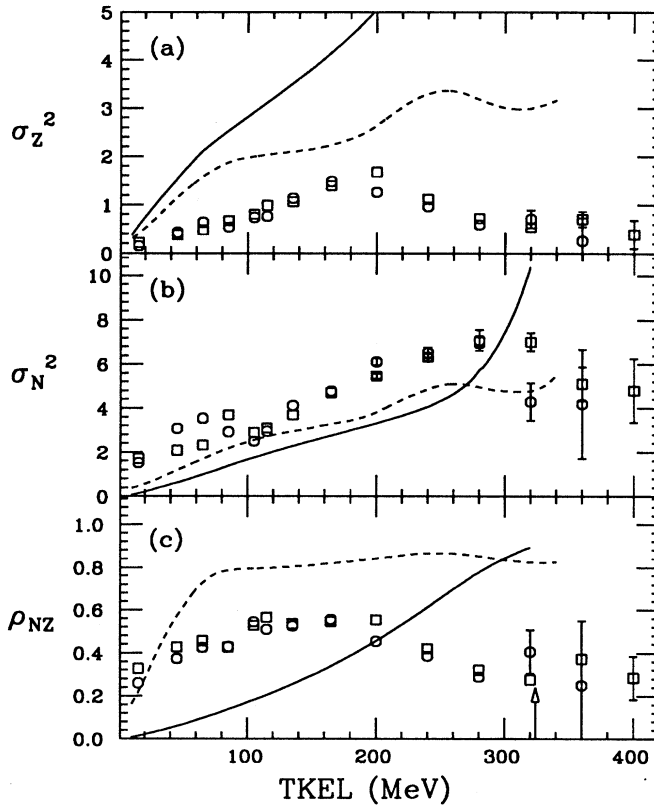


FIG. 5. Experimental and theoretical values for the variances  $\sigma_Z^2$  and  $\sigma_N^2$  and the correlation factor  $\rho_{NZ}$  corresponding to the secondary distributions of the projectilelike fragments. The circles and squares represent the experimental results after correcting the energy-loss scale, assuming equal and thermal division of the excitation energy, respectively. The theoretical results predicted by Randrup's and the Tassan-Got-Stéphan models are represented by lines. The dotted lines represent the theoretical calculations of the Tassan-Got-Stéphan model and the solid lines Randrup's predictions. The arrow indicates the limit imposed by the entrance channel spherical-Coulomb barrier.

nificant difference between the predictions of the two models for asymmetric systems. Given that the interaction-energy is related to kinetic terms such as the rotational energy, as well as to the potential surface energy of the interconnected nuclei, it is expected that the drift in Randrup's model leads the system towards mass symmetry. In the Tassan-Got-Stéphan model the mass and charge drifts are insensitive to the surface energy.

These models were implemented in computer codes and, after appropriate treatment of their output [9,10], primary distributions were generated. The evaporation of the primary fragments was performed using the code PACE [25] to obtain the secondary PLF's. The averages and variances were then calculated by moment analysis, as was done for the experimental data. The results for the  $\langle Z \rangle$ ,  $\langle N \rangle$ , and  $\langle N \rangle / \langle Z \rangle$  are shown in Fig. 4, where the long-dashed lines and the dash-dotted lines represent the result of the primary distributions predictions by Randrup's model and the Tassan-Got-Stéphan models, respectively. The solid lines represent the results from Randrup's model, and the short-dashed lines represent the results from the Tassan-Got-Stéphan model for the secondary distributions, after being corrected for evaporation using PACE II.

#### A. Drift and centroid distributions

Once the primary nucleon averages are defined, the secondary distributions are a function of the excitation energy distributions predicted by each model. In Fig. 6 the average excitation energy deposited in the projectilelike fragments

(a) and its proportion to the total excitation energy (b) as a function of TKEL are shown. The average excitation energy deposited in the primary PLF shows the same trend for both models, increasing steadily up to about 180 MeV, then decreasing from that value. The decrease of the excitation energy of the PLF [Fig. 6(a)] after reaching a maximum at around 230 MeV is to be related to the thermalization of the composite system, as can be seen in Fig. 6(b). Also, given that the maximum of the PLF's excitation energy is correlated to the change in the slope of  $\langle N \rangle$  and  $\langle Z \rangle$  at around the same interval of TKEL, it is likely the decrease in  $E_{PLF}^*$  is due to a saturation of the nucleon flow.

From the values of the excitation energy ratio, it can be seen that the total excitation energy of the system, as generated by the models, is approximately equally shared between the two fragments during the first 180 MeV of TKEL. After that the system tends towards a thermalized state with increasing energy loss. The fact that the ratio  $E_{PLF}^* / E_{tot}^*$  predicted by the Tassan-Got-Stéphan model is greater than 50% for small values of TKEL is likely because, according to this model, many nucleons transferred from the PLF to the TLF escape from the acceptor due to the high velocity mismatch, so that only part of the carried momentum is deposited into the TLF [19].

Given the average excitation energy predicted by Randrup's model and the Tassan-Got-Stéphan model, together with the measured secondary distributions, it is possible to use the iterative procedure described in Sec. III to reconstruct, from the measured experimental data, a reasonable

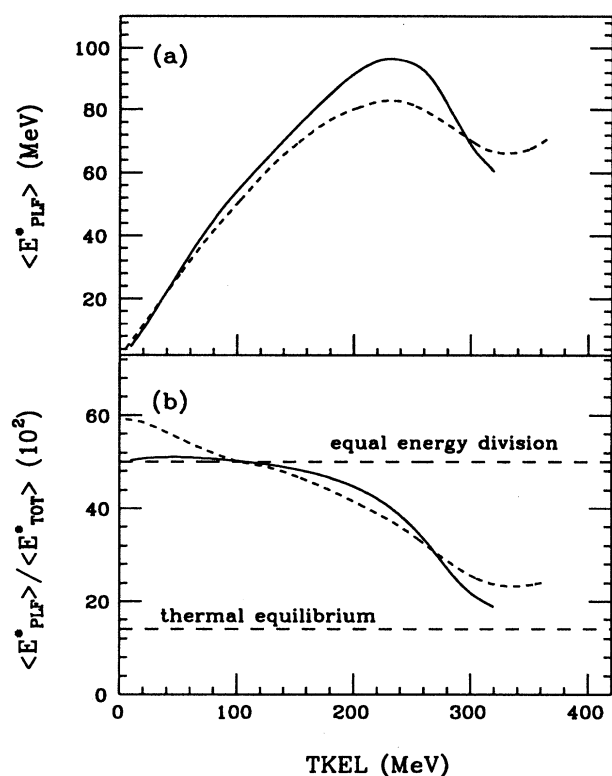


FIG. 6. Model calculations for the average excitation energy stored in the primary PLF (a) and percent ratio of the average excitation energy in the PLF to the average total excitation energy of the compound system (b) as a function of the TKEL. The dotted line refers to the Tassan-Got-Stéphan calculations, the solid lines represent Randrup's model prediction, and the dashed horizontal lines represent limits of equipartition of excitation energy and thermal equilibrium between the two reaction partners.

approximation of the average properties of the primary distributions of the projectilelike fragments. The results of this computation are shown in Fig. 7, where nucleon drifts (average measured atomic and neutron number minus the projectile atomic and neutron number) and the  $\langle N \rangle / \langle Z \rangle$  ratio of the primary fragments are plotted as function of the TKEL. The diamonds represent the reconstructed primary distributions using the excitation energy function supplied by Randrup's model. The corresponding distributions for the Tassan-Got-Stéphan model were not significantly different, and so they are not shown in this figure.

The drift values of the primary fragments shown in Fig. 7 indicate a net transfer of protons and neutrons from the projectile to the target. Up to 200 MeV of TKEL the proton transfer is small, with  $\langle Z \rangle - Z_p \approx 2$ . After this point the charge drift increases, with up to 8 protons transferred at 360 MeV of TKEL. Contrary to this evolution, the  $\langle N \rangle - N_p$  values decrease until 200 MeV of TKEL, where  $\langle N \rangle - N_p \approx 4$ , and then remain constant at around -6 neutrons. There is a corresponding change of sign of the slopes of the variances (Fig. 4) also around 200 MeV. Figure 7(c) shows the evolution of the  $N/Z$  ratio for the reconstructed primary distribu-

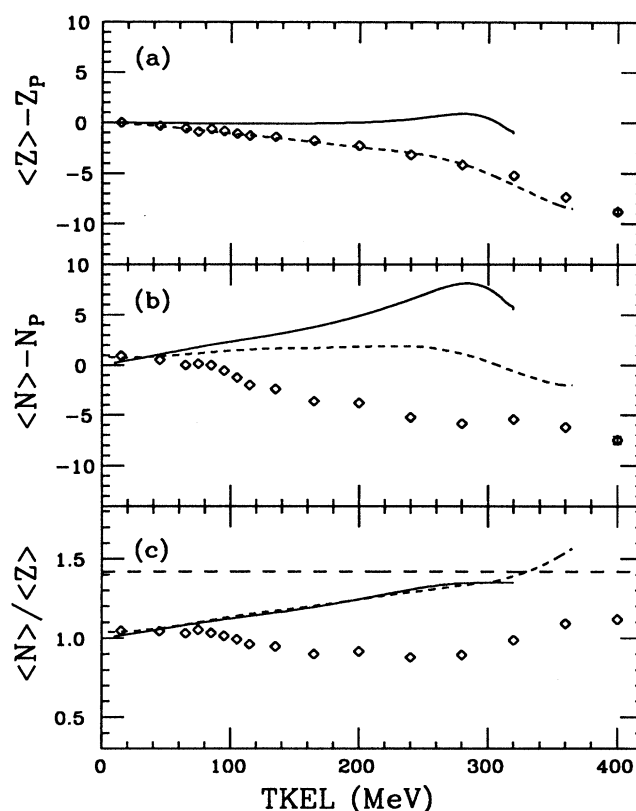


FIG. 7. Reconstructed and theoretical nucleon drift (average atomic and neutron number minus the projectile atomic and neutron number) and  $\langle N \rangle / \langle Z \rangle$  ratio for primary fragments, as function of the energy loss. The dotted and the solid lines represent primary distributions calculated with the Tassan-Got-Stéphan and Randrup's models, respectively. The dashed horizontal lines represent the value of the  $N/Z$  for the composite system. The arrow indicates the limit imposed by the entrance channel spherical-Coulomb barrier.

tions; as for the ratio of the secondary distributions, there is a tendency to maintain the  $N/Z = 1$  of the projectile.

In Fig. 7 the model predictions corresponding to the nucleon drift values for the primary distributions are also displayed. The dotted and solid lines represent the distributions calculated with the Tassan-Got-Stéphan model and Randrup's model, respectively. In both calculations, the  $\langle N \rangle / \langle Z \rangle$  evolution of the primary distributions exhibit a tendency of the system toward the neutron-to-proton ratio of the composite system. However, for each model this is achieved in different ways. In Randrup's model a net neutron transfer to the PLF increases steadily with TKEL, until it reaches its maximum at around 300 MeV, while the charge flow between the PLF and the TLF is almost nil. On the other hand, the Tassan-Got-Stéphan model produces a substantially smaller transfer of neutrons from the TLF to the PLF, compensated for by a strong charge flow in the opposite direction. The evolution of the proton drift of the reconstructed primary distributions is closer to the prediction by the Tassan-Got-Stéphan model; however, the neutron drift is overpredicted by this model. In the case of Randrup's pre-



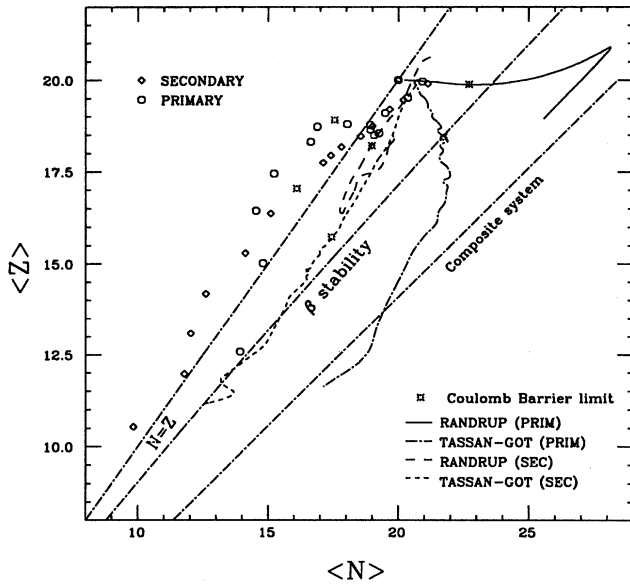


FIG. 8. Evolution of the nuclide distribution in the  $N$ - $Z$  plane of the projectilelike fragments as a function of TKEL. Experimental secondary distributions are represented by diamonds; reconstructed primary distributions are represented by circles. Primary and secondary distributions predicted by Randrup's model are indicated by solid and dashed lines, respectively. The calculated primary and secondary distributions for the Tassan-Got-Stéphan model are represented by dot-dashed and dotted lines, respectively. The stars on each line represent the corresponding limit of the TKEL imposed spherical entrance channel Coulomb barrier.

diction, both the neutron and proton drifts are overpredicted by the model.

The evolution in the  $N$ - $Z$  plane of the projectilelike fragment centroids is displayed in Fig. 8 for increasing values of TKEL. The centroids of the experimental distributions are represented by the circles for secondary and diamonds for primary fragments. Starting at the injection point of the initial system, the lines show the predictions of the Tassan-Got-Stéphan and Randrup's models. The composite system  $N/Z$ , the  $N=Z$ , and the  $\beta$  stability lines are also shown. In this figure, the stars on each line represent the corresponding limit of the TKEL imposed by the spherical entrance channel Coulomb barrier.

The primary distributions predicted by both models evolve towards the composite system line. However, the path followed by Randrup's prediction is driven by the mean field potential of the system and drifts toward symmetry, with a pronounced flow of neutrons to the PLF. For the Tassan-Got-Stéphan model, the path is the result of a localized interaction, as a result of a stochastic nucleon exchange. It is clear that, for both models, evaporation leads the distributions towards the valley of  $\beta$  stability, while the data only approach the  $N=Z$  line. For Randrup's secondary distributions, up to the first 230 MeV of TKEL, it looks as if the excess neutrons transferred from the TLF to the PLF during the iteration are the first to be evaporated, ending up close to the Tassan-Got-Stéphan secondary distributions. After the

230 MeV of TKEL, the secondary distributions predicted by Randrup's model considerably diverge from the data; at these energies the Tassan-Got-Stéphan prediction is a better match.

When comparing the evolution of the primary PLF's forecast by the models to the data, it would seem *a priori* that the data are closer to the Tassan-Got-Stéphan predictions than to Randrup's predictions. However, this assumption is hard to sustain after the evaporation, especially for lower values of TKEL. For TKEL greater than 230 MeV, it may be proposed that, as the system thermalizes (Fig. 6), a stochastic interchange of nucleons, as compared to a picture of exchanged nucleons driven by the mean field, is closer to the observed nucleon drift.

### B. Distribution variances

The model calculations for the secondary values of  $\sigma_Z^2$ ,  $\sigma_N^2$ , and  $\rho_{NZ}$  are displayed in Fig. 5. Both models predict an increase of the variances with energy loss. For  $\sigma_Z^2$ , Randrup's calculation diverges abruptly from the experimental results at the first few MeV of TKEL, increasing steadily up to 20 (off the scale of the figure) at around 320 MeV. The Tassan-Got-Stéphan predictions also overestimate the experimental values, although not by much. The values for  $\sigma_N^2$  better resemble the experimental distribution; however, both models underpredict the experimental results. It is interesting to note that both the  $\sigma_Z^2$  and  $\sigma_N^2$  values obtained from the Tassan-Got-Stéphan model appear to saturate at energy losses corresponding to the maxima of the excitation energy deposited in the primary PLF (Fig. 6). Finally, the  $\rho_{NZ}$  computed by Randrup's calculation increases steadily with TKEL. The evolution does not reflect at all the trend found for the data, underpredicting the experimental values up to 200 MeV of TKEL, after which it greatly overpredicts the same. On the other hand, the Tassan-Got-Stéphan prediction for  $\rho_{NZ}$  is consistently larger than that calculated from the data, for all but the lowest values of TKEL. Although the calculation does level off, it does so at a much larger value of  $\rho_{NZ}$  than the data show. Neither model predicts the decrease of the  $\rho_{NZ}$  after 200 MeV.

It is instructive to compare the evolution of the variances in terms of the data from studies at similar energies. The following experiments were used:  $^{37}\text{Cl} + ^{209}\text{Bi}$  at 15 MeV/n [10],  $^{58}\text{Ni} + ^{165}\text{Ho}$  at 16 MeV/n [28], and  $^{56}\text{Fe} + ^{165}\text{Ho}$  at 12 MeV/n [9]. Since the deep-inelastic mechanism evolves within the range of the total available kinetic energy, the TKEL scale between different systems is not equivalent. To perform a direct comparison between the systems, a rescaling of the TKEL was performed.

According to the nucleon exchange model [21], the energy loss per nucleon exchanged is proportional to the square root of the relative kinetic energy ( $T^{1/2}$ ), defined by

$$T^{1/2} = (E_{\text{c.m.}} - \text{TKEL} - V_C)^{1/2}, \quad (8)$$

where  $E_{\text{c.m.}}$  is the center-of-mass kinetic energy and  $V_C$  is the Coulomb barrier. Therefore, the initial relative kinetic energy of the system  $T_0^{1/2}$  is

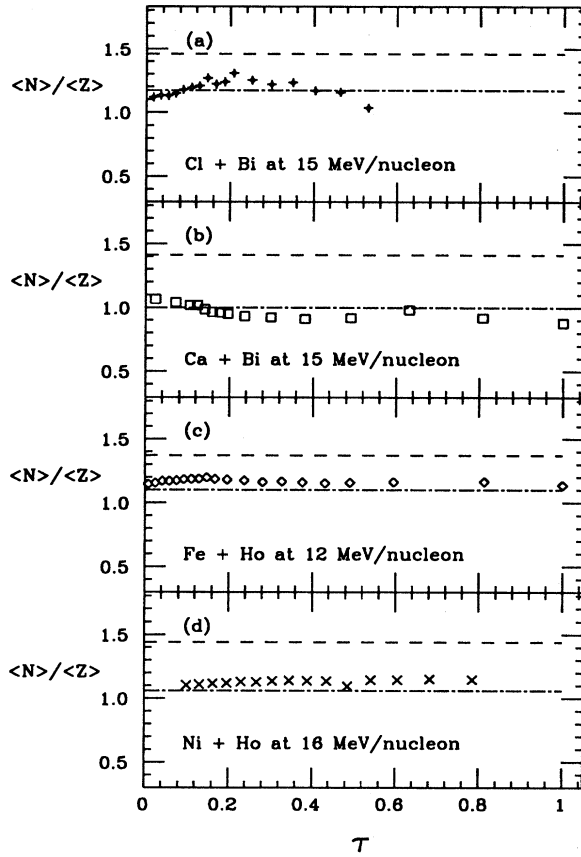


FIG. 9. Experimental values for the ratio  $\langle N \rangle / \langle Z \rangle$  as a function of the parameter  $\tau$ , corresponding to the secondary distributions of the projectilelike fragments for the systems (a)  $^{37}\text{Cl} + ^{209}\text{Bi}$  at  $E/A = 15$  MeV MeV/A [10], (b)  $^{40}\text{Ca} + ^{209}\text{Bi}$  at 15 MeV/A, (c)  $^{56}\text{Fe} + ^{165}\text{Ho}$  MeV/A [9], and (d)  $^{58}\text{Ni} + ^{165}\text{Ho}$  at 16 MeV/A [28]. The horizontal dash-dotted and dashed lines represent the  $N/Z$  values for each composite system and the  $N/Z$  of the correspondent PLF, respectively.

$$T_0^{1/2} = (E_{\text{c.m.}} - V_C)^{1/2}. \quad (9)$$

It is possible to rescale the TKEL by introducing the variable  $\tau$ ,

$$\tau = 1 - (T^{1/2}/T_0^{1/2}), \quad (10)$$

defined in the interval  $[0,1]$  from zero total kinetic energy loss to the limit of the kinetic energy available imposed by the exit channel Coulomb barrier, in this work approximated by that for the spherical entrance channel.

Figure 9 displays the values of  $\langle N \rangle / \langle Z \rangle$  as a function of  $\tau$  for the different systems. Also, in this figure the horizontal lines in each panel represent the  $N/Z$  value for each composite system and the  $N/Z$  of the correspondent PLF. For the systems Cl+Bi and Ni+Ho, the entire possible range of available energy was not reported, probably due to a lack of statistics for higher values of  $\tau$  (TKEL). As shown in Fig. 9

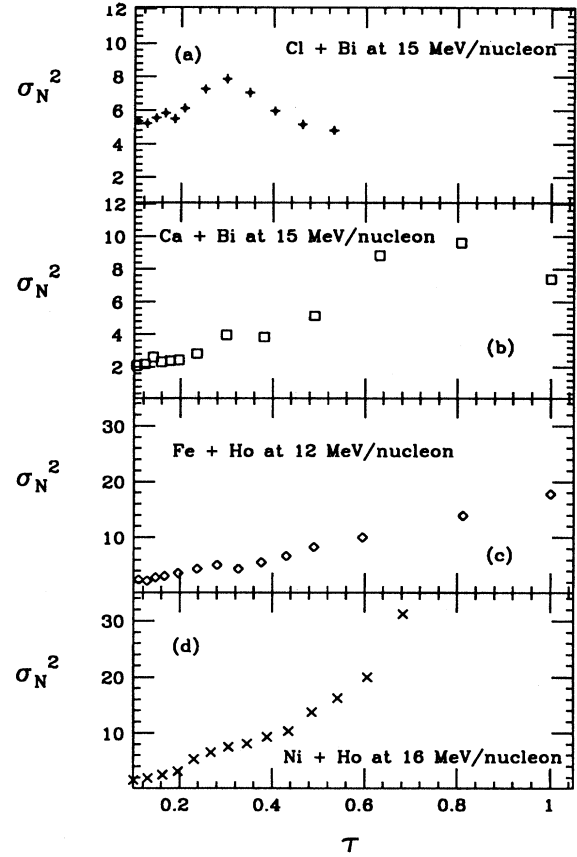


FIG. 10. Experimental values for the variances  $\sigma_N^2$  as a function of the parameter  $\tau$ , corresponding to the secondary distributions of the projectilelike fragments for the systems (a)  $^{37}\text{Cl} + ^{209}\text{Bi}$  at 15 MeV/n [10], (b)  $^{40}\text{Ca} + ^{209}\text{Bi}$  at 15 MeV/n, (c)  $^{56}\text{Fe} + ^{165}\text{Ho}$  at 12 MeV/n [9], and (d)  $^{58}\text{Ni} + ^{165}\text{Ho}$  at 16 MeV/n [28].

the ratio  $\langle N \rangle / \langle Z \rangle$  remains relatively constant as a function of  $\tau$  around the  $N/Z$  value of the correspondent PLF for all the systems. Given that the measured mass and charge are from evaporated fragments, it is difficult to give a direct interpretation to the  $N/Z$  trend observed.

Shown in Figs. 10 and 11 are the  $\sigma_N^2$  and  $\sigma_Z^2$ , respectively. It should be noted that as reported for the systems Cl+Bi [10], Ni+Ho [9], and as done for the system Ca+Bi, the width characterization of the distribution on the  $N$ - $Z$  plane was calculated via two methods. The first and second moments generated by a Gaussian fit were found to be equivalent to the corresponding widths calculated via moment analysis with the formulas described in Sec. I. This should minimize, in principle, any misrepresentation of the moment analysis.

The changes in magnitude of the variances for the different systems are remarkable, especially for the  $\sigma_N^2$  values, which have maximum values ranging from 10 at  $\tau$  around 0.6 units for the system Ca+Bi to about 35 units for the Ni+Ho system. The variances are not connected to the net number of nucleons transfer; this can be seen in Fig. 9. For example, at  $\tau$  around 0.28, we found that  $\sigma_N^2 \approx 7.85$  for  $\Delta N \approx 2$  (two neutrons transferred) for the system Cl+Bi, and

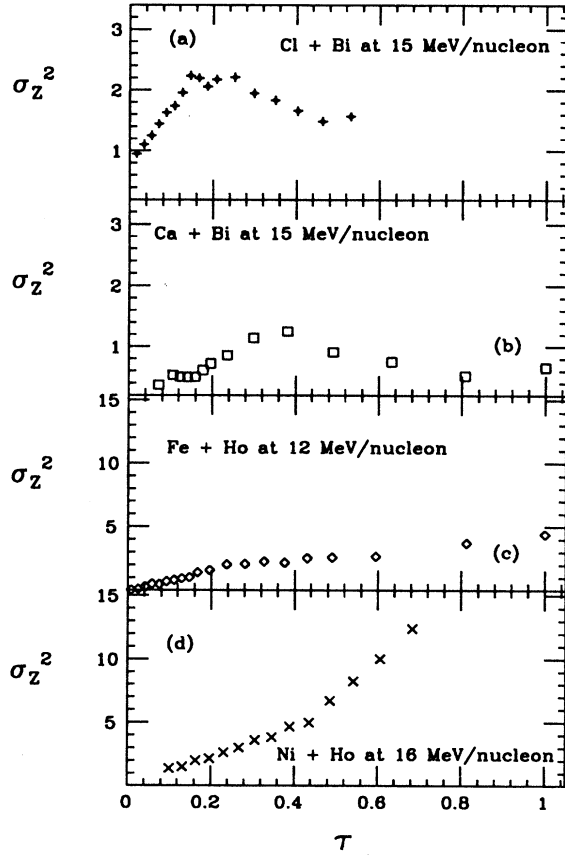


FIG. 11. Experimental values for the variances  $\sigma_Z^2$  as a function of the parameter  $\tau$ , corresponding to the secondary distributions of the projectilelike fragments for the systems (a)  $^{37}\text{Cl}+^{209}\text{Bi}$  at 15 MeV/n [10], (b)  $^{40}\text{Ca}+^{209}\text{Bi}$  at 15 MeV/n, (c)  $^{56}\text{Fe}+^{165}\text{Ho}$  at 12 MeV/n [9], and (d)  $^{58}\text{Ni}+^{165}\text{Ho}$  at 16 MeV/n [28].

$\sigma_N^2 \approx 6.56$ , for  $\Delta N \approx 3$  for the Ni+Ho system. While the drift must be a result of preferential nucleon exchange, the net driving force appears to be largely decoupled from the macroscopic exchange. The different ranges of the variances between systems as a function of TKEL have also been studied by de Souza *et al.* [16] without any conclusive results.

The general trend of the  $\sigma_N^2$  values (Fig. 10) is to increase as a function of  $\tau$ . However, the slope of this change shows a discontinuity, leading to a maximum for the Cl+Bi system and to an inflection point for the other systems at around 0.3 units of  $\tau$ . The  $\sigma_Z^2$  values (Fig. 11) seem to follow the same evolution, with an abrupt change in slope leading to maxima for the Cl+Bi and Ca+Bi systems, and to a clear inflection point for the other systems.

It is hard to give an interpretation of the evolution of the variances in the systems described, especially for the values where the neutron and charge variance begin decreasing. In the models discussed in this paper, an increase in the variances is correlated with an increase in the number of nucleons exchanged by the participant nuclei. The variances are expected to increase with increasing  $\tau$  or TKEL (proportional to the interaction time). Following this picture, a decrease in the variance, correlated with a change of slope of the drift,

may be interpreted as a reflection of a sudden decrease of nucleon flow. Furthermore, at around 0.4  $\tau$  units for Ca+Bi and 0.18 units for Cl+Bi [10], the models indicate that a transition from equal energy division to thermalization is also taking place, indication of some kind of saturation process for the deep-inelastic interaction. These observations, together with the decreasing of the correlation coefficient at the same energy region pointed out in Sec. III, could point to a different kind of interaction mechanism.

A breakup of the PLF is one possible explanation for these findings. In this picture, the tendency of the system towards the  $N=Z$  line, the evolution of the correlation coefficient, and the sudden change in the charge and neutron variances would be consistent with emission of alpha particles at some point during the interaction of the reaction partners [29]. The kinetic criteria of energy conversion may be explained within this mechanism given that it has been found that initial- or final-state interactions following breakup can lead to damped reaction processes involving one or both of the breakup fragments [30]. Finally, despite the fact that most of the studies that present evidence of an inelastic breakup process involve systems with relatively small projectiles, there is also evidence for breakup in heavier alpha-conjugate nuclei [31].

## V. SUMMARY AND CONCLUSIONS

The mass and charge distributions for the secondary PLF's from the reaction  $^{40}\text{Ca}+^{209}\text{Bi}$  at  $E/A = 15$  MeV have been measured. The distributions have been parametrized in terms of the first and second moments as a function of the TKEL. Presuming evaporation mechanisms for correction of the TKEL, the primary distributions for the PLF have been reconstructed, using the division of the excitation energy between the participant nuclei as predicted by Randrup's model. The evolution of the centroids, variances, and correlation coefficients with the TKEL has been compared to the predictions from the Tassan-Got-Stéphan and Randrup's models. The trends of the charge and neutron variances have been compared to the variances of the distributions found in other experiments.

From the  $\langle N \rangle / \langle Z \rangle$  experimental values, it is clear that there is a strong tendency of the PLF to maintain the neutron-to-proton ratio of the original projectile up to very high values of TKEL. As a result, an intense flow of protons can be observed from the PLF to the TLF, together with a small net transfer of neutrons in the same direction.

For the second moments, a small correlation between the charge and the neutron number is observed, in agreement with the Tassan-Got-Stéphan model. On the other hand, the variances show a peculiar tendency to decrease after reaching a maximum. The same behavior is found when comparing this evolution with the trends of the variances for other systems. This together with an evolution of the centroids and drifts towards the  $N=Z$  may be a sign that the system is driven, not only by a deep-inelastic-like reaction mechanism, but may be also influenced by processes such as projectile fragmentation or breakup.

The recent surge in experimental techniques using  $4\pi$  and forward angle detection systems seems ideal to confirm these findings or to study alternative mechanisms for damped reactions. The forward detectors would be able to detect alpha-particle breakup fragments in coincidence. Also the detection of the targetlike fragments using a  $4\pi$  array would permit the reconstruction of the primary fragments.

## ACKNOWLEDGMENTS

The authors wish to thank L. Tassan-Got and J. Randrup for providing the computer codes based on their models. This research was supported by the U.S. Department of Energy under Grants No. DEFG05-87ER40321 and No. DEFG02-93ER40802.

- 
- [1] W.U. Schröder, J.R. Birkelund, and J.R. Huizenga, *Phys. Rev. Lett.* **36**, 514 (1976).
  - [2] J. Randrup, *Nucl. Phys.* **A327**, 490 (1979).
  - [3] H. Breuer, B.G. Glagola, V.E. Viola, K.L. Wolf, A.C. Mignerey, J.R. Birkelund, D. Hilscher, A.D. Hoover, J.R. Huizenga, W.U. Schröder, and W.W. Wilcke, *Phys. Rev. Lett.* **43**, 191 (1979).
  - [4] H. Breuer, A.C. Mignerey, V.E. Viola, K.L. Wolf, J.R. Birkelund, D. Hilscher, J.R. Huizenga, W.U. Schröder, and W.W. Wilcke, in *Proceedings of the IXth International Workshop on Gross Properties of Nuclei and Nuclear Excitations*, Hirschegg, Austria, 1981 (unpublished), p. 162.
  - [5] H. Breuer, A.C. Mignerey, V.E. Viola, K.L. Wolf, J.R. Birkelund, D. Hilscher, J.R. Huizenga, W.U. Schröder, and W.W. Wilcke, *Phys. Rev. C* **28**, 1080 (1983).
  - [6] R.A. Broglia, C.H. Dasso, and A. Winther, *Phys. Lett.* **53B**, 301 (1974); **61B**, 113 (1976).
  - [7] R. Planeta, K. Kwiatowski, S.W. Zhou, V.E. Viola, H. Breuer, M.A. McMahan, W. Kehoe, and A.C. Mignerey, *Phys. Rev. C* **41**, 3942 (1990).
  - [8] T.C. Awes, R.L. Ferguson, R. Novotny, F.E. Obenshain, F. Plasil, S. Pontoppidan, V. Rauch, G.R. Young, and H. Sam, *Phys. Rev. Lett.* **52**, 251 (1984).
  - [9] H. Madani, A.C. Mignerey, A.A. Marchetti, A.P. Weston-Dawkes, W.L. Kehoe, and F. Obenshain, *Phys. Rev. C* **51**, 2562 (1995).
  - [10] A.A. Marchetti, A.C. Mignerey, H. Madani, A. Gökmen, W.L. Kehoe, H. Breuer, K. Wolf, and F. Obenshain, *Phys. Rev. C* **48**, 266 (1993).
  - [11] B. Gatty, D. Guerreau, M. Lefort, J. Pouthas, X. Tarrango, J. Galin, B. Cauvin, J. Girard, and H. Nifenecker, *Z. Phys. A* **273**, 65 (1973).
  - [12] U. Brosa and H.J. Krappe, *Z. Phys. A* **284**, 65 (1978).
  - [13] U. Brosa and D.H.E. Gross, *Z. Phys. A* **298**, 91 (1980).
  - [14] E.S. Hernandez, W.D. Myers, J. Randrup, and B. Remaud, *Nucl. Phys.* **A361**, 483 (1981).
  - [15] D.H.E. Gross and K.K. Hartmann, *Phys. Rev. C* **24**, 2526 (1981).
  - [16] R.T. de Souza, W.U. Schröder, J.R. Huizenga, J. Toke, S.S. Datta, and J.L. Wile, *Phys. Rev. C* **39**, 114 (1989).
  - [17] D.K. Lock, R. Vandenboch, and J. Randrup, *Phys. Rev. C* **31**, 1268 (1985).
  - [18] J. Randrup, *Nucl. Phys.* **A383**, 468 (1982).
  - [19] L. Tassan-Got and C. Stéphan, *Nucl. Phys.* **A524**, 121 (1991).
  - [20] A. Menchaca-Rocha, E.J. Garcia-Solis, E. Belmont, and M.E. Brandan, *Phys. Rev. C* **45**, 1189 (1992).
  - [21] W.U. Schröder and J.R. Huizenga, in *Treatise on Heavy Ion Science*, edited by D.A. Bromley (Plenum, New York, 1984), Vol. 2, p. 149.
  - [22] *Computer and Acquisition Handbook of the HHIRF*, Oak Ridge National Laboratory, Oak Ridge, Tennessee, 1987.
  - [23] LISA Collaboration, H. Breuer *et al.*, University of Maryland Report, 1989.
  - [24] A.A. Marchetti and A.C. Mignerey, *Nucl. Instrum. Methods A* **324**, 288 (1993).
  - [25] A. Gavron, *Phys. Rev. C* **21**, 230 (1980).
  - [26] D.R. Benton, H. Breuer, F. Khazaie, K. Kwiatkowski, V. Viola, S. Bradley, A.C. Mignerey, and A.P. Weston-Dawkes, *Phys. Lett. B* **185**, 326 (1987).
  - [27] D.R. Benton, H. Breuer, F. Khazaie, K. Kwiatkowski, V. Viola, S. Bradley, A.C. Mignerey, and A.P. Weston-Dawkes, *Phys. Rev. C* **38**, 1207 (1988).
  - [28] V. Penumetcha, G.A. Petitt, T.C. Awes, J.R. Beene, R.L. Ferguson, F.E. Obenshain, F. Plasil, G.R. Young, and S.P. Sorensen, *Phys. Rev. C* **42**, 1489 (1990).
  - [29] P.L. Gonthier, J.D. Lenters, M.Y. Vonk, T. Koppenol, D.A. Cebra, W.K. Wilson, A. Vander Molen, J. Karn, S. Howden, A. Nadasen, J.S. Winfield, and G.D. Westfall, *Phys. Rev. C* **43**, 504 (1991).
  - [30] J. Wilczyński, K. Siwek-Wilczyńska, J. Van Driel, S. Gonggrijp, D.C.J.M. Hageman, R.V.F. Janssens, J. Lukasiak, R.H. Simssen, and S.Y. van Der Werf, *Nucl. Phys.* **A371**, 109 (1982).
  - [31] A. Gamp, J.C. Jacmart, N. Poffé, H. Doubre, J.C. Roynette, and J. Wilczynski, *Phys. Lett.* **74B**, 215 (1978).